

The evolution substructure I: a new identification method

Stuart P. D. Gill, Alexander Knebe, Brad K. Gibson

Centre for Astrophysics & Supercomputing, Swinburne University, Mail #31, P.O. Box 218, Hawthorn, Victoria, 3122, Australia

Received ...; accepted ...

ABSTRACT

We describe our new “MLAPM-halo-finder” (MHF) which is based on the adaptive grid structure of the N -body code MLAPM. We then extend the MHF code in order to track the orbital evolution of gravitationally bound objects through any given cosmological N -body-simulation - our so-called “MLAPM-halo-tracker” (MHT). The mode of operation of MHT is demonstrated using a series of eight high-resolution N -body simulations of galaxy clusters. Each of these halos hosts more than one million particles within their virial radii r_{vir} . We use MHT as well as MHF to follow the temporal evolution of hundreds of individual satellites, and show that the radial distribution of these substructure satellites follows a “universal” radial distribution irrespective of the host halo’s environment and formation history. This in fact might pose another problem for simulations of CDM structure formation as there are recent findings by Taylor et al. (2003) that the Milky Way satellites are found preferentially closer to the galactic centre and simulations underestimate the amount of central substructure, respectively. Further, this universal substructure profile is anti-biased with respect to the underlying dark matter profile. Both the halo finder MHF and the halo tracker MHT will become part of the open source MLAPM distribution.

Key words: methods: n-body simulations – methods: numerical – galaxies: formation – galaxies: halos

1 INTRODUCTION

Over the last 30 years great progress has been made in the development of N -body codes that model the distribution of dissipationless dark matter. Algorithms have advanced considerably since the first N^2 particle-particle codes (Aarseth 1963; Peebles 1970; Groth et al. 1977); we have seen the development of the tree-based gravity solvers (Barnes & Hut 1986), mesh-based solvers (Klypin & Shandarin 1983), then the two combined (Efstathiou et al. 1985) and multiple strands of adaptive and deforming grid codes (Villumsen 1989; Suisalu & Saar 1995; Kravtsov, Klypin & Khokhlov 1997; Bryan & Norman 1998; Knebe, Green & Binney 2001). While they all push the limits of efficiency in computational resources, each code has its individual advantages and limitations. The result of such research has been highly reliable, cost effective codes. However, producing the data is only one step in the process; the ensembles of millions of (dissipationless) dark matter particles generated still require interpreting and then comparison to the real Universe. This necessitates access to analysis tools to map the phase-space which is being sampled by the particles onto “real” objects in the Universe; traditionally this has been accomplished through the use of “halo finders”. Halo finders mine N -body data to find locally over-dense gravitationally bound systems, which

are then attributed to the dark halos we currently believe surround galaxies. Such tools have led to critical insights into our understanding of the origin and evolution of structure and galaxies. To take advantage of sophisticated N -body codes and to optimise their predictive power one needs an equally sophisticated halo finder.

Over the years, halo-finding algorithms have paralleled the development of their partner N -body codes. We briefly outline the major halo finders currently in use:

The Friends-of-Friends (FOF) (Davis et al. 1985; Frenk et al. 1988) algorithm uses spatial information to locate halos. Specifying a linking length b_{link} the finder links all pairs of particles with separation equal to or less than b_{link} and calls these pairs “friends”. Halos are defined by groups of friends (friends-of-friends) that have at least one of these friendship connections. Two such advantages of this algorithm are its ease of interpretation and its avoidance of assumption concerning the halo shape. The greatest disadvantage is its simple choice of linking length which can lead to a connection of two separate objects via so-called linking “bridges”. Moreover, as structure formation is hierarchical, each halo contains substructure and thus the need for different linking lengths to identify “halos-within-halos”. There have been many variants to this scheme which attempt to overcome some of these limitations (Suto, Cen & Ostriker

arXiv:astro-ph/0404258v1 13 Apr 2004

1992; Sugimotohara & Suto 1992; van Kampen 1995; Okamoto & Habe 1999; Klypin et al. 1999).

DENMAX (Bertschinger & Gelb 1991; Gelb & Bertschinger 1994a) and SKID (Weinberg, Hernquist & Katz 1997) are similar methods in that they both calculate a density field from the particle distribution, then gradually move the particles in the direction of the local density gradient ending with small groups of particles around each local density maximum. The FOF method is then used to associate these small groups with individual halos. A further check is employed to ensure that the grouped particles are gravitationally bound. The two methods differ through their calculation of the density field. DENMAX uses a grid while SKID applies an adaptive smoothing kernel similar to that employed in Smoothed Particle Hydrodynamics techniques (Lucy 1977; Gingold & Monaghan 1977; Monaghan 1992). The effectiveness of these methods is limited by the method used to determine the density field (Götz, Huchra & Brandenberger 1998).

A similar technique to the above is the Bound Density Maxima (BDM) method (Klypin & Holtzman 1997; Klypin et al. 1999). In this scheme a smoothed density is derived by smearing out the particle distribution on a scale r_{smooth} of order the force resolution of the N -body code used to generate the data. Randomly placed “seed spheres” with radius r_{smooth} are then shifted to their local centre-of-mass in an iterative procedure until convergence is reached. Hence, as with DENMAX and SKID, this process finds local maxima in the density field. Bullock et al. (2001) further refined the BDM technique by first generating a set of possible centres, ranking the particles with respect to their local density and then implementing modifications which allow for credible identification of halos-within-halos. The Bullock et al. (2001) adaptation to BDM excels at finding halo substructure.

When one is primarily concerned with distinct halos, all the mentioned methods perform exceedingly well. All efforts to refine and enhance those halo finding algorithms are due to the fact that N -body codes overcame overmerging only recently (Klypin et al. 1999) and are capable of finding satellite galaxies within dark matter host halos. It is therefore crucial to reliably identify “halos-within-halos”. In fact, one of the remaining problems for simulations of CDM structure formation is that high-resolution simulations nowadays predict far greater substructure (in total) than observed (Klypin et al. 1999; Moore et al. 1999). Results from gravitational microlensing suggest that the majority of substructure which does exist has to be close to the inner regions (Dalal & Kochanel 2002) which thus far has not been confirmed by such simulations. There are recent claims that although the overmerging problem has disappeared in the outer regions of the halo, the inner regions might still suffer from it (Taylor, Silk & Babul 2003). As these latter semi-analytic models do not suffer from such numerical problems, they find that such substructure does exist in the inner regions. The question though arises as to whether there still remains an overmerging problem in the simulations or if current halo finding algorithms actually do break down at those scales. As we will discuss later, it becomes more difficult to locate peaks in the central region (if at all present) of the host halo due to a simple lack of contrast.

In this paper we present a new method for identifying gravitationally bound objects in N -body code output that

uses the adaptive meshes of MLAPM (Knebe et al. 2001). This new code excelled at finding “halos-within-halos” revealing more substructure in the inner regions of the host halo. In its native form, our new algorithm works naturally “on-the-fly”, but it has also been constructed with the flexibility necessary to handle a single temporal output from any N -body code. Our analysis software will become part of the publicly available MLAPM distribution*. The outline of the paper is as follows. In Section 2 we introduce the cosmological models used to frame our discussion of the mode of operation of the new halo finder and tracker. A more detailed scientific analysis of this data set can be found in Paper II of this series (Gill et al. 2004a; hereafter, GKGDII). In Section 3 we introduce the new halo finder “MLAPM-halo-finder” (MHF), describing its function, advantages, and limitations. Section 4 provides a brief analysis of the satellites found by MHF. In Section 5 we introduce the “MLAPM-halo-tracker” (MHT) which augments the halo finder by incorporating the ability to track the temporal evolution of satellites. Analysis of the halos tracked with MHT is described in Section 6. We next compare the two methods with other publicly available halo finding algorithms, such as FOF and SKID, in Section 7. We conclude with a summary and our conclusions in Section 8.

This paper is the first in a series of three based upon the suite of simulations described herein. Paper II (GKGDII) investigates the satellite environments and their dynamical properties, while Paper III (Gill et al. 2004b) will investigate the tidal streams and debris from the disrupting satellites.

2 SIMULATION DETAILS

The N -body simulations presented in this and the companion papers were carried out using the open source adaptive mesh refinement code MLAPM (Knebe et al. 2001). MLAPM reaches high force resolution by refining high-density regions with an automated refinement algorithm. These adaptive meshes are recursive: refined regions can themselves be refined, each subsequent refinement having cells that are half the size of the cells in the previous level. This creates a hierarchy of refinement meshes of different resolutions covering regions of interest. The refinement is done cell-by-cell (individual cells can be refined or de-refined) and meshes are not constrained to have a rectangular (or any other) shape. The criterion for (de-)refining a cell is simply the number of particles within that cell and a detailed study of the appropriate choice for this number can be found elsewhere (Knebe et al. 2001). The code also uses multiple time steps on different refinement levels where the time step for each level is a factor of two smaller than the time step on the previous level. The latest version of MLAPM also includes an adaptive time stepping that adjusts the actual time step after every major step to restrict particle movement across a cell to a particular fraction of the cell spacing, hence, improving the accuracy and computational time.

We first created a set of four independent initial conditions at redshift $z = 45$ in a standard Λ CDM cosmology ($\Omega_0 = 0.3, \Omega_\lambda = 0.7, \Omega_b h^2 = 0.04, h = 0.7, \sigma_8 = 0.9$). Next,

* <http://astronomy.swin.edu.au/MLAPM/>

Table 1. Summary of the eight host dark matter halos. Distances are measured in h^{-1} Mpc, velocities in km s^{-1} , masses in $10^{14}h^{-1} M_{\odot}$, and the age in Gyrs.

Halo	R_{vir}	$V_{\text{circ}}^{\text{max}}$	M_{vir}	z_{form}	age	$N_{\text{sat}}(< r_{\text{vir}})$
# 1	1.34	1125	2.87	1.16	8.30	158
# 2	1.06	894	1.42	0.96	7.55	63
# 3	1.08	875	1.48	0.87	7.16	87
# 4	0.98	805	1.10	0.85	7.07	57
# 5	1.35	1119	2.91	0.65	6.01	175
# 6	1.05	833	1.37	0.65	6.01	85
# 7	1.01	800	1.21	0.43	4.52	59
# 8	1.38	1041	3.08	0.30	3.42	251

512^3 particles were placed in a box of side length $64h^{-1}$ Mpc giving a mass resolution of $m_p = 1.6 \times 10^8 h^{-1} M_{\odot}$. For each of these initial conditions we iteratively collapsed the closest eight particles to one particle reducing our particle number to 128^3 particles. These lower mass resolution initial conditions were then evolved until $z = 0$.

At $z = 0$, eight clusters from our simulation suite were selected in the mass range $1-3 \times 10^{14} h^{-1} M_{\odot}$, each sampling differing environmental conditions. Then, as described by Tormen et al. (1997), for each cluster the particles within two times the virial radius were tracked back to their Lagrangian positions at the initial redshift ($z = 45$). Those particles were then regenerated to their original mass resolution and positions, with the next layer of surrounding large particles regenerated only to one level (i.e. 8 times the original mass resolution), and the remaining particles were left 64 times more massive than the particles resident with the host cluster. This conservative criterion was selected in order to minimise contamination of the final high-resolution halos with massive particles.

At the end of the high-resolution re-simulations the force resolution is determined by the highest refinement level reached. The whole computational volume was covered by a regular domain grid consisting of 256^3 cells. We had two separate criteria for refinement, a domain cell was refined when there was more than one particle per cell, further, every subsequent refinement was refined when there was more than four particles per cell. Thus the finest grid at $z = 0$ consisted of 65,536 cells per side, giving a force resolution of $\approx 2h^{-1}$ kpc which allows us to resolve the host halos down to the central $\sim 0.25\%$ of the virial radii of the host halos (see Table 1).

The halos chosen were selected to investigate the evolution of satellite galaxies and their debris in an unbiased sample of host halos, exploring the influence of environment upon the evolution of such systems. To achieve this goal, excellent temporal resolution is required - as such we retained 17 outputs from $z = 2.5$ to $z = 0.5$, equally spaced with $\Delta t \approx 0.35$ Gyrs, supplemented with an additional 30 outputs spanning $z = 0.5$ to $z = 0$ with $\Delta t \approx 0.17$ Gyrs. As we show in a companion paper (Gill et al. 2004), the average number of orbits for our satellites is of the order 1-2. Therefore we have approximately 10-20 outputs available to define the orbit of a satellite, which is more than adequate to follow a live orbit properly. We found that to sufficiently sample a live satellite orbit you need at least eight time-steps. As you

increase the time sampling the stability of the result quickly converges.

A simple analysis of the simulation at redshift $z = 0$ provides us with the relevant information on the host halo. At $z = 0$ the halo masses range from $1-3 \times 10^{14} h^{-1} M_{\odot}$ where the mass was defined to be the total mass within the virial radius R_{vir} , double counting both substructure and sub-substructure. The virial radii in turn were defined at the point where the mean averaged density of the host (measured in terms of the cosmological background density ρ_b) drops below $\Delta_{\text{vir}} = 340$ with M_{vir} being the mass enclosed by that sphere. We then follow Lacey & Cole (1994) and use their definition for formation time: the formation redshift z_{form} is the redshift where the halo contains half of its present day mass. Applying this criterion to our data we find that the ages of our host halos have a spread ranging from roughly 8.3 Gyrs to as young as 3.4 Gyrs. This alone shows that we are dealing with dynamically different systems even though their masses are comparable; our older halo's substructure has nearly twice the time to relax than the youngest one's satellites. A summary of the eight host halos is presented in Table 1 where the halos are presented and numbered from oldest to youngest. The variation in the number of satellites from halo to halo with a trend for smaller hosts to contain less satellites can be accounted for by the mass cut applied to the satellites; as we expect a shift in the substructure mass function to lower masses for smaller hosts we are artificially cutting off satellites by applying a constant lower mass limit of $10^{10} h^{-1} M_{\odot}$.

3 MHF: MLAPM'S HALO FINDER

The general goal of a halo finder is to identify gravitationally bound objects. As all halos are centered about local over-density peaks they are usually found simply by using the spatial information provided by the particle distribution. Thus, the halos are located as peaks in the density field of the simulation. To locate objects in this fashion, the halo finder is required in some way to reproduce the work of the N -body code in the calculation of the density field or the location of its peaks. When locating halos like this, the major limitation will always be the appropriate reconstruction of the density field. With that in mind we introduce MLAPM's-Halo-Finder, MHF (or simply Finder) hereafter.

MHF essentially uses the adaptive grids of MLAPM to locate the satellites of the host halo. As previously mentioned in Section 2, MLAPM's adaptive refinement meshes follow the

density distribution *by construction*. Grid structure naturally “surrounds” the satellites, as the satellites are simply manifestations of over-densities within (and exterior) to the underlying host halo, a view which can best be appreciated through inspection of Figure 1. In this figure, the refinement grids of MLAPM are superimposed over the projected density of the particle distribution. The top image is the 5th refinement level, with the 6th and 7th levels shown below. We emphasise that the grids get successively smaller and are subsets of other grids on lower refinement levels. The advantage of reconstructing and using these grids to locate halos is that they naturally follow the density field with the *exact* accuracy of the N -body code. No scaling length is required, in contrast with techniques such as FOF. Therefore, MHF avoids one of the major complications inherent to most halo finding schemes as a natural consequence of its construction.

To locate appropriate halos within our simulation outputs we first build a list of “potential centres” for the halos. Using the full adaptive grid structure invoked by MLAPM, with the same refinement criterion as for the original runs, we restructure the hierarchy of nested isolated MLAPM grids into a “grid tree” and generate a list of prospective halo centres by storing the centroid of the densest grid at the end of each grid tree’s “branch”. Assuming that each of these peaks in MLAPM’s adaptive grids is the centre of a halo, we step out in (logarithmically spaced) radial bins until the density reaches $\rho_{\text{satellite}}(r_{\text{vir}}) = \Delta_{\text{vir}}(z)\rho_b(z)$, where ρ_b is the universal background density, unless we reach a point r_{trunc} where an upturn in the radial density profile is detected. This rise is encountered for (almost) all satellites embedded within the background density of the host halo, a point that we will discuss in more detail in Section 4. The outer radius of the satellite is defined to be either r_{vir} or r_{trunc} , whichever is smaller, and dubbed r_{MHF} . Using all particles interior to r_{MHF} we calculate other canonical properties for each halo such as its mass, rotation curve, and velocity dispersion.

We now, however, need to prune the list of (still prospective) halos by removing gravitationally unbound particles and duplicate halos. The latter occurs in two steps - first, for each satellite a set of “duplicate candidates” is constructed based on the criterion that their centres lie within each others’ outer radii r_{MHF} . Second, this list is then checked by comparing the internal properties of the candidates. A candidate was affirmed to be a duplicate once its mass, velocity dispersion, and center of mass velocity vector agreed to within 80%. We then kept the halo with the higher central density and removed the other one from the satellite catalogue completely. This is a rare circumstance, yet one to which we will return in Section 4. With our nearly complete set of halos now in hand, we proceed to remove gravitationally unbound particles. This again is done in an iterative process. Starting with the MHF halo centre, we calculate the kinetic and potential energy for each individual particle in the respective reference frame and all particles faster than two times the escape velocity are removed from the halo. We then recalculate the centre, and proceed through the process again. This pruning is halted when a given halo holds fewer than eight particles or when no further particles need to be removed. We finish by recalculating the internal properties of the halos with the radial density profiles of the satellites fitted to

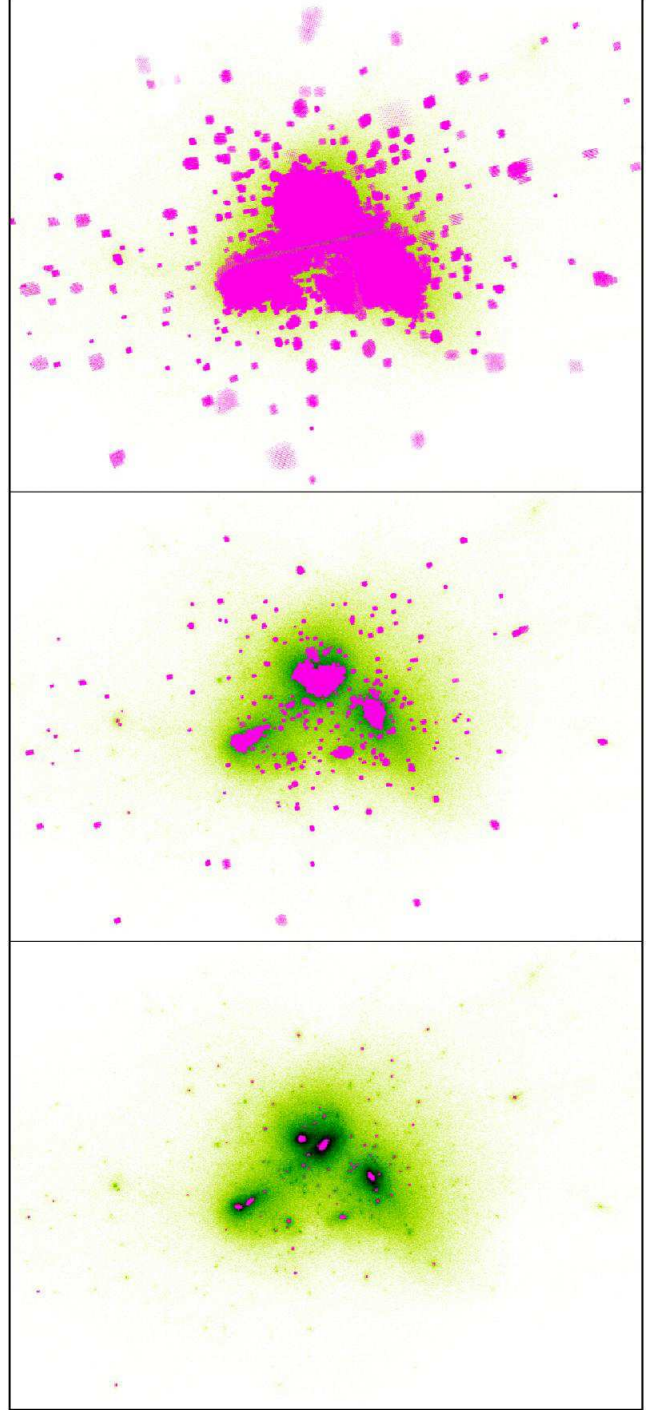


Figure 1. This panel shows a series of 3 consecutive refinement levels of MLAPM’s grid structure starting at the 5th refinement level superimposed upon the density projection of the particle distribution.

the functional form proposed by Navarro, Frenk & White (1997; hereafter, NFW)

$$\rho^{\text{cum}}(r) = \frac{M(<r)}{\frac{4\pi}{3}r^3} \propto \frac{1}{(r/r_s)(1+r/r_s)^2}. \quad (1)$$

in the range from $8h^{-1}$ kpc ($\approx 4\times$ force resolution) to r_{MHF} .

The scale radius r_s is used to define the concentration of the halo

$$c = r_{\text{vir}}/r_s. \quad (2)$$

The procedure outlined above naturally deals with overlapping halos and substructure halos, respectively. But as mentioned before, for such objects the virial radius can not be determined properly as we will observe a rise in the radially binned density profile due to the overlap with another halo or the embedding into the host. In that case we set the outer radius of the (sub-)halo to be that point where the density profile rises and all canonical properties are derived using all (gravitationally bound!) particles interior to that radius. And the fit to an NFW profile Equation (1) is only done out to that radius, too. The situation is different once both of the overlapping halo's centres are within each other's virial/upturn radius: we then checked, if those two objects are just duplicates by comparing their internal properties.

As stated in Section 2, it is our aim to investigate the evolution of satellite galaxies within their host halos. Thus, we restrict our satellites to having at least 50 high-resolution simulation particles, which corresponds to a mass-cut of $M_{\text{cut}} \approx 10^{10} h^{-1} M_{\odot}$. Moreover, each satellite must contain at least 50% percent of its mass in high-resolution particles. In practice, this latter constraint is not a critical one, relevant only for satellites beyond twice the host halo's virial radius.

We can further take advantage of the MLAPM grids for measuring the triaxiality of regions surrounded by an isodensity contour. Essentially the various refinement levels are cuts in the density field (isodensity surfaces). We calculated the inertia tensor for each isolated refinement, weighting each cell by its density. Then using the eigenvalues of the inertia tensor we construct the triaxiality parameter (Franx, Illingworth & Zeeuw 1991)

$$T = (a^2 - b^2)/(a^2 - c^2). \quad (3)$$

To describe the host halo's triaxiality we used the 6th refinement level in MLAPM. According to the refinement criterion adopted in the simulations the 6th level surrounds material about 3000 times denser than ρ_b or, in other words, nine times denser than the material at the virial radius. A density of roughly $9 \times \rho(r_{\text{vir}})$ corresponds to approximately the half-mass radius of the host.

MHF is implemented into MLAPM in a way that provides the user simultaneously with a snapshot of the dark matter particles *and* halo catalogues at each required output. The most obvious advantages of having the analysis performed “on the fly” are the reduction in computer and human hours in the initial halo analysis stage. Embedding the halo analysis in the code also enables us to potentially analyse the data at unprecedented time resolution, if required.[†] However, MHF can also be used with any already existing single time-step snapshot and hence is not limited to data produced by MLAPM; it can also be used for any N -body output provided the latter is converted to MLAPM's binary format using the tools included in the MLAPM distribution.

[†] MHF can be switched on either to act only when writing an output file (-DMHF) or at each individual time step (-DMHFstep).

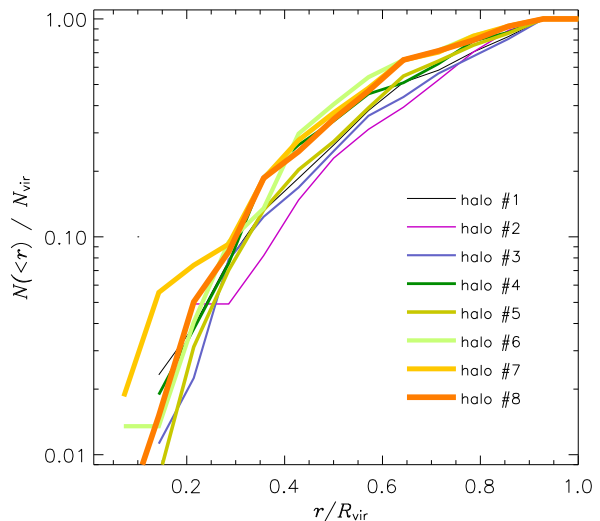


Figure 2. Number of satellites (normalised) orbiting within the virial radius of the host halo at $z = 0$, as a function of radial distance r , normalised by the virial radius of the respective host R_{vir} .

4 ANALYSIS OF MHF HALOS

MHF was applied to each of the 376 temporal outputs (47 outputs per each of the eight independent halos), providing us with a list of all satellites and their internal properties at each individual redshift under consideration. As stated earlier, the detailed analysis of the science associated with this study is presented in Paper II (GKGDII). We do however wish to highlight several key preliminary results here which relate specifically to the halo identification process.

In Figure 2 we plot the normalised number of satellites as a function of normalised radius. One, perhaps not surprising, aspect of Figure 2 is the similarity in the slopes. Although the number of satellites in each halo may vary, the relative radial distribution of the satellites is similar across halos. This is reminiscent of the universal density profile of dark matter halos, as described by NFW. Although the radial distribution of the satellites remains consistent, there exists a range of substructure densities for the halos, as there is a spread in the number of satellites within each halo (recall Table 1). Therefore, we should be able to distinguish the effects of substructure density on the physical properties of the satellites.

The other striking feature of Figure 2 is the lack of satellites in the inner 15% of the virial radius. One might ask why this is the case. Does it indicate that satellites dynamically avoid the central region of the halo? Perhaps they simply do not spend much time there? Perhaps via physical means satellites that venture near the centre are either merged or experience such strong tidal forces that they are destroyed? Perhaps we are simply dominated by numerical effects and are witnessing the premature destruction of halos in dense environments. This latter problem - known as *overmerging* - affected low-resolution dissipationless simulations in the early 1990s, failing to produce galaxy-sized dark matter halos in clusters (e.g. Summers et al. 1995; van Kampen 1995; Moore et al. 1996). Traditionally, this was explained by the

lack of dissipation in the simulations. With the inclusion of a baryonic component, denser objects could form and survive in the centres of these dense regions. However, with the onset of higher resolution simulations a converse effect was encountered - specifically, an *abundance* of substructure was found (Klypin et al. 1999).

The explanation of overmerging (or substructure disruption) was accredited to numerical limitations in the simulations. van Kampen (1995) found that particle evaporation due to two-body effects is only important for low particle number halos (<30 particles). Moore et al. (1996) further investigated particle halo heating, which they concluded was negligible should sufficient mass resolution exist. Moore et al. also demonstrated the for satellites in a static host potential, if a simulation had insufficient spatial resolution, halos would have artificially large cores and hence undergo accelerated tidal disruption. They also found that halos become unstable and are erased when the tidal radius is smaller than approx 2-3 times the halo core radius (which itself can be related to the gravitational softening length). Klypin et al. (1999) investigated the issue of “overmerging” in great detail using a variety of higher resolution simulations, concluding that the resolution required to avoid artificial destruction of galaxy-sized halos of mass $\approx 10^{11} h^{-1} M_{\odot}$ was $\leq 2 h^{-1}$ kpc (spatial) and $\leq 10^9 h^{-1} M_{\odot}$ (mass).

Since we appear to have sufficient numerical resolution and our data lies well within the limits of not being dominated by overmerging, one might query whether or not the lack of substructure in the inner region is due to a limitation of our halo finder. When defining the radius of our halos we could not for all halos follow the density profiles out to r_{vir} defined via $\rho_{\text{sat}}(r_{\text{vir}}) = \Delta_{\text{vir}} \rho_b$; as noted earlier, it was necessary in many cases to define a truncation radius r_{trunc} . The existence of r_{trunc} generally indicates that the satellite is embedded within the host’s density field, as already noted by Bullock et al. (2001). Thus, as a satellite gets closer to the central density region of the host halo, its overdensity peak becomes less contrasted. It is intrinsically harder to find satellites with low central densities under the standard paradigm of halo finding, especially close to the cuspy centre. It is not at all obvious how to disentangle the particle distribution of the satellite and the host halo: this is a fundamental limit to finding halos in the traditional way of observing over-densities and requires further investigation. In the next section, however, we introduce a method of finding halos that eliminates the background halo and, hence, minimises this problem.

The MHF method fails in the inner regions for two reasons. Firstly, because it is hard to detect the upturn in the density field, substructure is eliminated through suspected duplication of a halo because the substructure’s radius has been falsely tracked out to essentially the virial radius of the host, its own upturn radius has been missed. The second reason results from a fundamental flaw in MHF’s methodology - that the smaller satellite grids merge with the host’s refinement grid and hence do not produce an isolated refinement. Therefore we are losing potential centres, a problem illustrated further in Figure 3. There, we show the inner $250 h^{-1}$ kpc of halo #1, along with the grids for the 7th refinement level of MLAPM (gray-shaded areas) with the central refinement about $60 h^{-1}$ kpc in radius. The dark spheres in-

dicate the positions of satellites located by MHF. Note that those dark spheres that do not encompass an isolated refinement grid would do so at one of the next coarser (or finer) levels. The light sphere at the border of the ellipsoidal host refinement also surrounds a satellite galaxy. However, this object was *not* picked up by the **Finder** but rather by the **Tracker** outlined in the next section. MHF was unable to identify this satellite as an individual object as its refinement grid has merged with the host’s grid, thus not allowing an isolated refinement and a potential center, respectively. The straight line pointing to this satellite is simply its orbital path.

The problem can be viewed differently in Figure 4. Here we plot the radially averaged density of the host halo at the position of a satellite against the maximum, central density of the satellite itself for redshift $z = 0$. The results are presented for the **Finder** (crosses) as well as for the **Tracker** (diamonds) to be introduced in Section 5. The line running through the plot for each individual host halo marks the 1:1 correspondence: satellites that fall onto (or even above) this line have central densities equal to (or smaller than) the host environment they are embedded within. We do observe a general (and reasonable) trend for satellites to have higher central densities than their dark matter vicinity. However, the figure also proves that the **Tracker** tends to also find satellites less contrasted and closer to the 1:1 relation, respectively. When interpreting Figure 4, and especially comparing the **Finder** to the **Tracker** results, one needs to bear two things in mind: firstly, there are many more **Tracker**-satellites obscuring a one-to-one comparison with **Finder**, and secondly, **Finder** relies on r_{MHF} as the final point of the profile whereas **Tracker** has the ability to properly measure r_{vir} . Minor differences in binning can also lead to very small changes in the central density calculation.

5 MHT: MLAPM’S HALO TRACKER

Conventional halo finders have a rich history in identifying isolated systems. In this regard, MHF might be viewed as simply an alternative approach to an already reasonably well-understood problem. To be fair though, MHF does push the conventional paradigm of simply using the three dimensional spatial data to locate the halos to the limit, locating the halos with (nearly) the exact accuracy of the N -body code. Having this ability, MHF becomes the ideal halo finder to locate substructure for MLAPM and no doubt an excellent halo finder for other codes. Although, as we have seen in Section 4, apart from numerical limitations in N -body codes (e.g. overmerging) there still remain limitations to our current halo finders. These limitations become a problem in the simulations when considering the substructure of any dense system, for example galaxy clusters and galaxies. Therefore, to successfully find the substructure we need to change the paradigm used to find it.

To successfully make this change we must first understand the environment in which we are finding the substructure and then exploit its characteristics. One characteristic is that most halos conserve their identities, that is substructure halos rarely undergo mergers in halos because of their high relative velocities (Ghigna et al. 1998; Okamoto & Habe 1999). Further, halos in dense environments undergo tidal

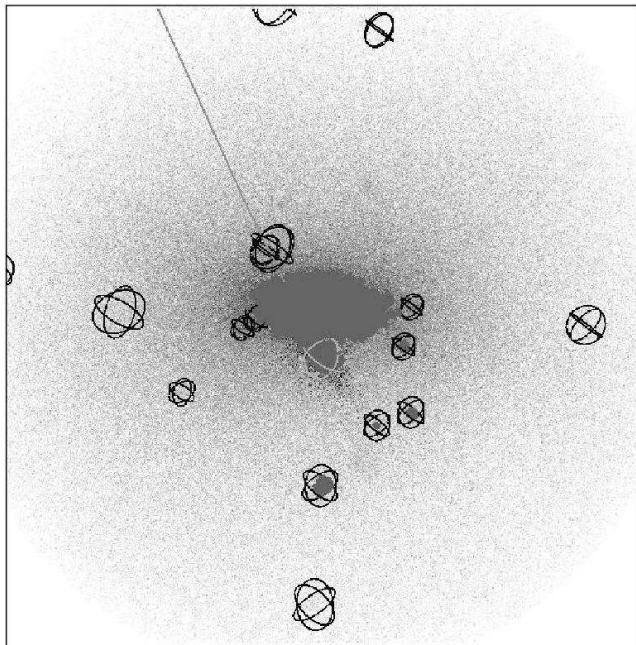


Figure 3. The inner $250 h^{-1}$ kpc of halo #1 with the particles’ line of sight density shown. We show the grids of the 7th refinement level of MLAPM, with the central refinement about $60 h^{-1}$ kpc in radius. The dark spheres represent the satellites located by MHF. The light sphere surrounds a satellite galaxy not found by MHF. The apparent sizes of the spheres are simply a visualisation effect as spheres farther away from the virtual observer appear smaller.

stripping and substructure interactions, no longer accreting material, but being stripped of it. Thus in such environments it is sufficient to trace the particles of the satellite once the satellite has entered the host’s virial radius. In this section we introduce MLAPM’s-Halo-Tracer, MHT (or simply **Tracker**) hereafter.

MHT takes an arbitrary output of our new MLAPM-based halo finder MHF, and correlates the particles for an arbitrary number of time steps using all simulation outputs from that initial output until redshift $z = 0$. In our particular investigation it was appropriate to define that initial arbitrary output to be the formation time z_{form} of the host halo or the time when the host halo contained half of its present mass (Lacey & Cole 1994). We then followed all the satellites that were within two times the virial radius of the host halo at this formation time. Although, we miss a few satellites due to MHF’s identification limitations in the inner 10-15% of the halo, from this time on MHT precisely follows the orbits of our initial set of satellites irrespective how close they come to the host’s centre. Explicitly, MHT takes the particles from an initial MHF analysis and then locates these particles in the next available output again. **Tracker**’s first task is then to (re-)calculate the halo’s centre. This is done by using the centre-of-mass of the innermost 20 particles from the previous time step as an initial estimate, then using the same iterative method to check the credibility of the halo, as outlined in Section 3. Once the satellite was identified as bona fide the radial profile was generated, a NFW profile fitted, and other canonical properties calculated. The binning for the profile again used logarithmically spaced radial bins covering the entire particle distribution. The ra-

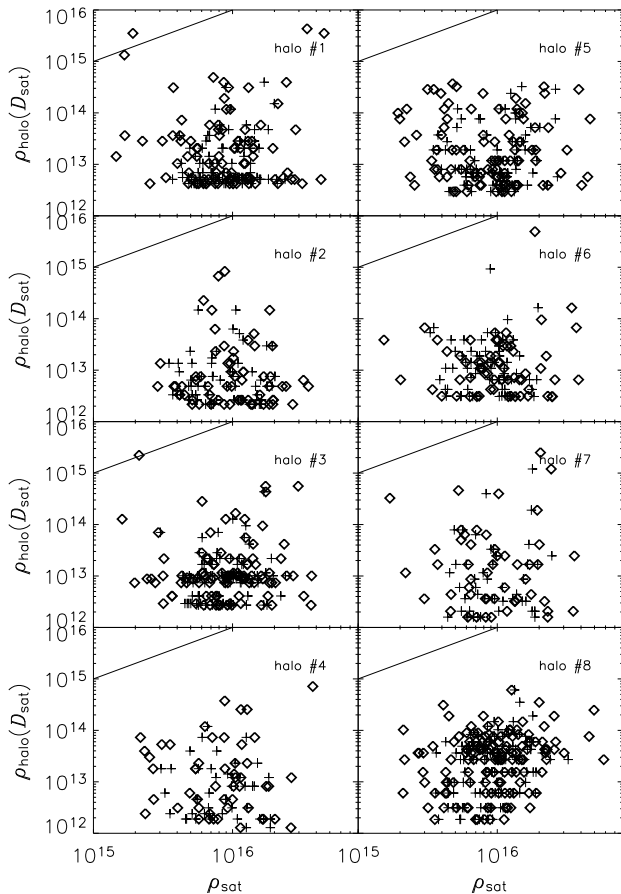


Figure 4. The density of the host halos at the radial distance D_{sat} of the satellite versus the central density of the satellites. The crosses represent the satellites found by **Finder** while the diamonds are the satellites found by **Tracker**.

dius of the satellite was consistently determined as being the radius when the cumulative density profile dropped below $\rho_{\text{satellite}}(r_{\text{vir}}) = \Delta_{\text{vir}}(z)\rho_b(z)$. This time we will not encounter the situation where the profile rises again as is the case for **Finder**; the satellite is no longer embedded within the “particle background” of the host halo but treated as a separated entity.

There are a number of advantages in tracing the halos in this way - first, because we are tracking just the satellites’ individual particles we do not have the complication of the background density distribution and the consequent lack of contrast against the host system for all outputs $z < z_{\text{form}}$. Following from this, we do not have to accept the truncation radius - the radius where the **Finder** encounters and upturn in the density profile - as the “natural” radius of the satellite. Further, this method allows us to investigate the development of tidal streams, which forms the basis of the extensive analysis provided in Paper III.

6 ANALYSIS OF MHT HALOS

The nature of hierarchical structure formation, i.e. mergers, dynamical and tidal destruction of substructure, requires a

little more work when applying MHT to our simulation data. Even though we are now tracing the initially bound particles forward in time, we need a criterion to decide whether a satellite galaxy is disrupted or still alive. We therefore introduce the tidal radius as given below.

6.1 Tidal Radius

The tidal radius is defined to be the radius of the satellite where the gravitational effects of the host halo are greater than the self-gravity of the satellite. When approximating the host halo and the satellite as point masses and maintaining that the mean density within the satellite has to be three times the mean density of the host halo within the satellites distance D to the host halo (Jacobi limit) the definition for tidal radius reads as follows

$$r_{\text{tidal}} = \left(\frac{m}{3M} \right)^{\frac{1}{3}} D, \quad (4)$$

where m is the mass of the satellite and $M = M(< D)$ is the mass of the host halo internal to the distance D .

In order to stabilise the determination of the tidal radius r_{tidal} we actually use an iterative procedure again. By defining the satellite mass m as the mass internal to r_{tidal} , i.e. $m = m(< r_{\text{tidal}})$, we find r_{tidal} by solving

$$r_{\text{tidal}} - \left(\frac{m(< r_{\text{tidal}})}{3M} \right)^{\frac{1}{3}} D = 0. \quad (5)$$

Starting with the distance of the furthest particle in the satellite particle distribution as the initial guess for r_{tidal} , the method quickly converges in only two-to-three iterations.

6.2 Satellite Disruption

As the satellites orbit within the host halo they undergo tidal stripping, hence, the satellites are gradually losing mass. Therefore, their particle distribution becomes more and more diffuse, reducing the tidal radius of the satellite. Eventually there comes a point when the satellite loses sufficient mass that we begin to reach the limits of our numerical resolution, not having sufficient number of particles to follow the satellite further. The satellite might have survived for longer, however, we do not have the resolution to follow it. Thus when a satellite passes through our numerical limit we tag it “disrupted”. In practice this means that if there are fewer than 15 particles within the tidal radius we classify the satellite as being disrupted. Note that we are unable to separate numerical resolution disruption and real physical disruption of a satellite. It is not clear if we had infinite mass resolution that the satellite would still actually survive.

We also stress that since our tidal radius formulae assumes circular orbits, the usual D corresponds to the pericentric distance (Hayashi et al. 2003); however, we calculate r_{tidal} for each satellite at each individual output to check for (tidal) disruption.

Furthermore, particles outside the tidal radius are not automatically stripped from the halo - what is just as important is the time spent under the influence of that tidal field, it still takes time for the particle to climb out of the potential. For example a satellite might be on a very eccentric orbit and pass close to the centre of the host halo, thus

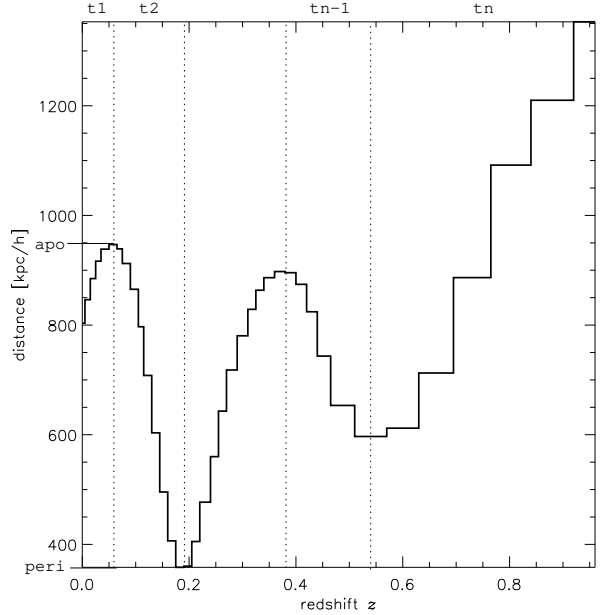


Figure 5. Distance from the center of the host halo in real coordinate system as a function of redshift for one particular satellite with $(M_{\text{sat}}/M_{\text{host}} = 0.7 \times 10^{-2})$.

having a very small tidal radius at the pericentre. Now it is true that most of the tidal stripping will occur at this pericentre, however, because the satellite only spends a short time there not all the particles outside the tidal radius will be stripped.

6.3 Orbital Information

In GKGDII we present a detailed analysis of the satellites’ orbits, but do take the opportunity here to provide some basic terminology relevant to both Papers I and II here. The high temporal resolution of our simulations ($\Delta t = 0.17$ and $\Delta t = 0.35$ Gyrs, respectively, for $z > 0.5$ and $z < 0.5$) enables us to track in detail the orbits of the satellites. As an example, in Figure 5 we show the orbit of one particular satellite. We can see that this satellite initially plunged in from outside the virial radius at $z = 0.8$ and was subsequently captured by the host, undergoing two further orbits prior to $z = 0$. This orbital information was then used to construct a measure of eccentricity

$$\epsilon = 1 - \frac{p}{a} \quad (6)$$

where p is the most recent “closest” distance to the host’s centre as a minima (labelled **peri** in Figure 5) and a the most recent “furthest” distance (labelled **apo**) as a maxima. Moreover, we are also in the position to calculate the number of orbits from the time evolution of the distance to the host centre. To this extent, we simply count the number of extrema (four in the case shown) and divide by two. We further correct for incomplete orbits at the beginning and end points of the distance relation, resulting in the following formula for the total number orbits:

$$N_{\text{orbits}} = \frac{N_{\text{extrema}}}{2} + \min\left(\frac{1}{2}, \frac{t_1}{t_2}\right) + \min\left(\frac{1}{2}, \frac{t_n}{t_{n-1}}\right) \quad (7)$$

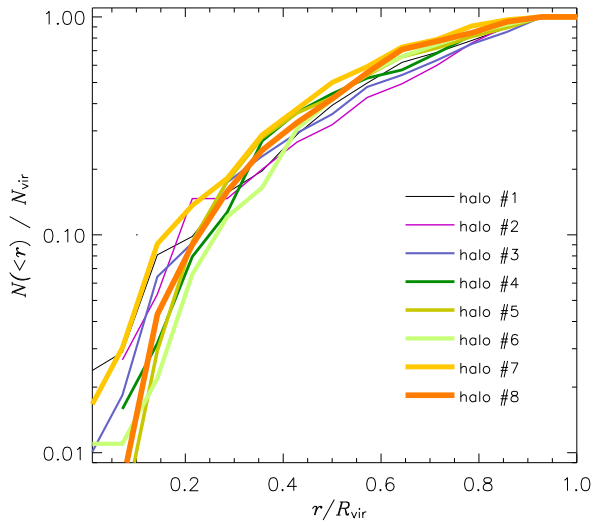


Figure 6. Number of satellites within a particular radius normalised by the total number of satellites as a function of radius normalised by the virial radius at $z = 0$. Only satellites more massive than $2 \times 10^{10} h^{-1} M_{\odot}$ were taken into account.

The number of orbits measured by that method for the sample satellite presented in Figure 5 is $N_{\text{orbits}} = 2.69$.

We emphasise though that the orbits of the satellites are not always as aesthetically “smooth” as that for the one presented in Figure 5. We are dealing here with live potentials and hundreds of satellites orbiting within it simultaneously. The host halo is constantly growing in mass and shows internal oscillations in shape due to ongoing mergers (see GKGDI). This has an impact on the orbital evolution of the satellites, as described in Paper II.

6.4 The radial distribution of satellites

In Figure 2 we showed the radial distribution of satellites for MHF. We now present in Figure 6 the same plot for MHT highlighting the superiority of the **Tracker**. Once again we observe the similarity in the slopes across the eight halos, a so-called “universal satellite distribution”. However, the important result is that using the **Tracker** we now find (more) objects within the central 10% of r_{vir} of the host halos. For halo #1, for instance, we located 5 satellites with mass greater than $10^{10} h^{-1} M_{\odot}$ within 10% of the virial radius with the closest satellite at $z = 0$ being a mere $35 h^{-1}$ kpc away from the host’s centre.

To allow a more natural comparison to work published by other authors, we present the data in a slightly different fashion in Figure 7. This time the radial number density of satellite galaxies is shown. As with Ghigna et al. (2000) and De Lucia et al. (2003) we also find that the subhalo population is “anti-biased” relative to the dark matter distribution in the inner regions of the halos. Moreover, we again observe no trend with environment for the sample of eight halos under investigation; all halos, irrespective of age and richness, do show the same anti-bias in the satellite distribution.

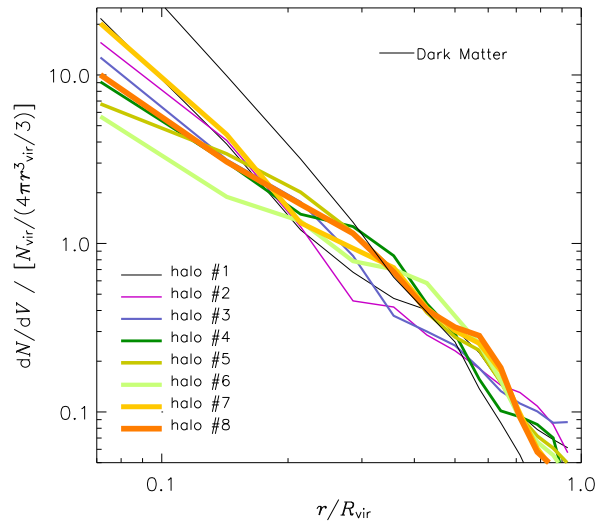


Figure 7. Number density of satellites normalised by the average number of satellites per unit volume as a function of radius normalised by the virial radius at $z = 0$. Only satellites more massive than $2 \times 10^{10} h^{-1} M_{\odot}$ were taken into account.

7 COMPARISON TO OTHER HALO FINDERS

In this section we compare MHF and MHT to two other halo finders, namely SKID and FOF. In Figure 8 we present a visual comparison of the effectiveness of the respective halo finders. Firstly, the top two panels show the line of sight density projection of particles for halo #1 within a $700 h^{-1}$ kpc sphere. The left panel displays all the particles, while the right panel only shows every third particle. In the remaining four panels, we present the results of the halo finding algorithms: (reading clockwise, starting upper left) MHT, SKID, FOF, and MHF. A sphere of fixed radius $20 h^{-1}$ kpc surrounds each located satellite where different apparent sizes are simply visualisation effects, i.e. spheres farther away from the virtual observer appear smaller.

SKID was run with multiple linking lengths and the option to remove gravitationally unbound particles enforced.[‡] Under close visual inspection, the best SKID results were found with linking lengths $b=0.03$ & $b=0.05$ times the inter-particle separation. The same values were taken for the FOF analysis. The results from the analysis with linking length $b=0.05$ [§] appear to be the most reliable ones and hence are shown in Figure 8. We need to stress though that the analysis of the SKID and FOF results can be further refined by combining various halo catalogues into a tree as explained in, for instance, Ghigna et al. (2000). However, one of the benefits our MLAPM halo finders is that neither requires any further input such as a linking length. Moreover, the latest version of MLAPM is capable of performing the analysis “on-the-fly”. A visual inspection of Figure 8 indicates that

[‡] For a detailed description of SKID please refer to <http://www-hpcc.astro.washington.edu/tools/skid.html>.

[§] A linking length of $b=0.05$ expressed in terms of the inter-particle separation translates into a physical linking length of $\sim 6 h^{-1}$ kpc, which is roughly three times the force resolution.

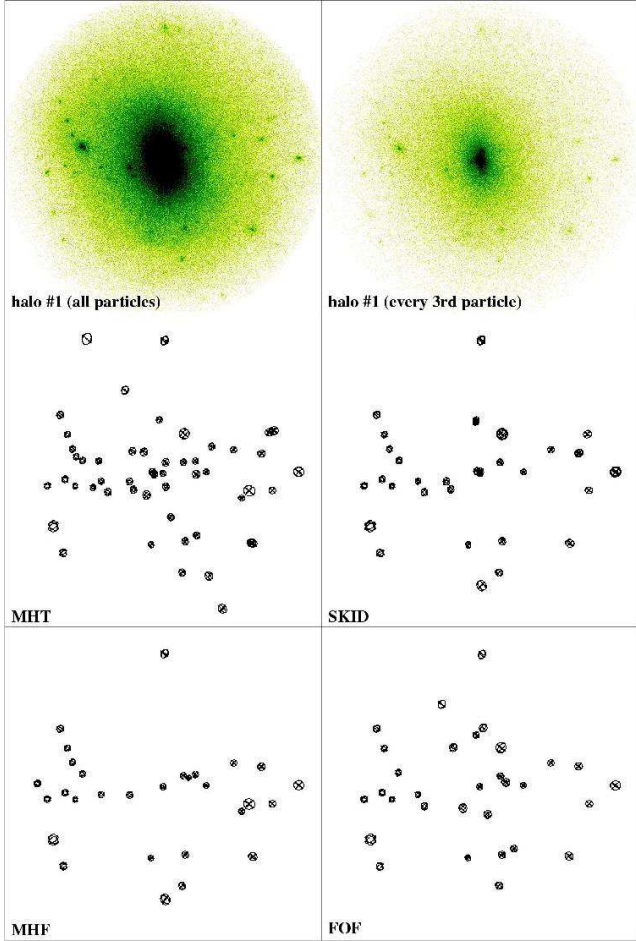


Figure 8. The top two panels show the line of sight density projection of particles for halo #1. The left panel displays all the particles, while the right panel shows every third particle. The remaining four panels show the results of the halo finding algorithms: MHT, SKID, FOF, and MHF (clockwise from top left). A sphere of fixed radius $20h^{-1}$ kpc surrounds each satellite.

MHT provides the most complete halo list. Specifically, the **Tracker** found 53 satellites, the **Finder** found 32, SKID 33 and FOF 32 within the plotted spherical region of diameter $1.4h^{-1}$ Mpc. Within the sets of satellites, there is of course considerable overlap. Essentially, each set of satellites found by MHF, SKID, and FOF were subsets of MHT. To look at this quantitatively, we calculate the radial number density of satellites for all four halo finders again (cf. Figure 7). This time we concentrate on halo #1 highlighting the differences between the halo finding methods. The result is presented in Figure 9 which clearly shows the success of the **Tracker** over all other methods. However, it is interesting to note that a simple FOF analysis gives quantitatively similar results to the more sophisticated SKID data. The difference between the **Finder** and the **Tracker** is quite remarkable, as is the similarity between MHF and SKID with $b=0.03$. Our explanation for the lack of substructure in the central region for this particular SKID analysis is that these objects were either removed because of our lower mass cut of 100 particles or the fact that SKID did not classify them as gravitationally bound. What we can also learn from Figure 9 is that the sensitivity of the halo finder in the inner regions can severely

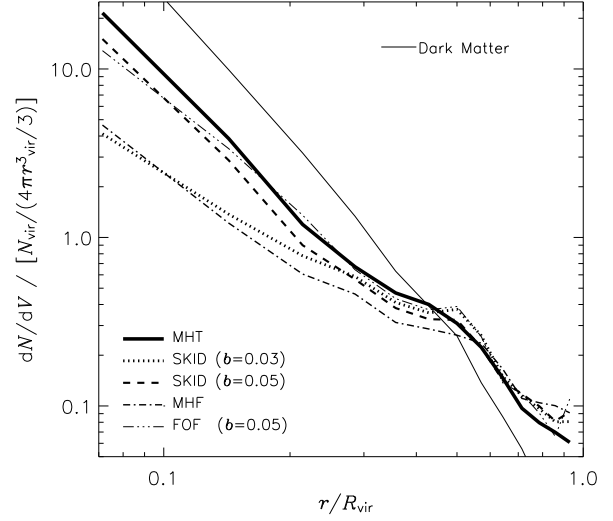


Figure 9. Number density of satellites normalised by the average number of satellites per unit volume as a function of radius normalised by the virial radius at $z=0$, halo #1 for each of the halo finding algorithms: MHT, SKID, MHF, FOF. Only satellites more massive than $2 \times 10^{10} h^{-1} M_{\odot}$ were taken into account.

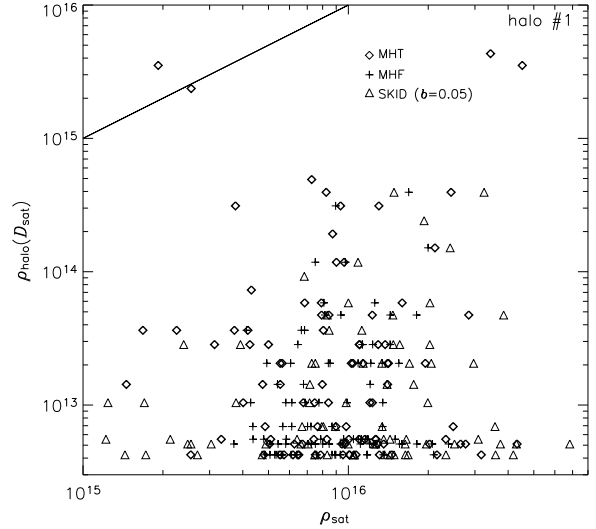


Figure 10. Same as Figure 4, but this time comparing **Tracker** (diamonds) and **Finder** (crosses) with the SKID, $b=0.05$ (triangles) analysis for halo #1.

bias the results. For example using MHF or SKID with $b=0.03$ provides a much stronger anti-bias in the satellite distribution than the more appropriate **Tracker** and SKID ($b=0.05$) analysis, respectively.

We like to close the comparison by coming re-examining Figure 4, this time including the results from the SKID ($b=0.05$) analysis. The result for halo #1 can be viewed in Figure 10. We still observe that *only* the **Tracker** is capable of resolving satellites with central densities close to the (local) density of the host halo. We also inspected the situation for the FOF ($b=0.05$) data and could not find any

significant difference and hence decided to not plot the data for clarity.

8 CONCLUSIONS

Computational cosmology is not only limited by crucial factors such as the dynamical range and the mass resolution, but also by its analysis tools. We emphasise, perhaps obviously to most readers, that N -body codes simulating structure formation in the Universe can only ever be as useful as their associated analysis tools allow.

In this paper we presented two new methods for identifying gravitationally bound objects in such simulations. Both methods are based upon the open source adaptive mesh refinement code MLAPM (Knebe et al. 2001). They both exploit the refinement hierarchy of said code and hence locate halos as well as halos-within-halos with exactly the same accuracy as MLAPM simulates their evolution. We showed the limitations of a simple snapshot analysis and how it can be overcome by taking into account the whole history of each halo. Thus not restricting the halo finding algorithm to just the spatial information but rather including the velocity information as well, hence, using the full six-dimensional information available.

Not only do we intend to implement the halo finder into the distribution of MLAPM allowing for an on-the-fly analysis saving both computational and human resources in the analysis process, but it is also our intention to have it as a stand alone program. In both cases, the implementation will be such that it can analyse a single output of any given N -body code.

We showed that halo finding still possesses the inherent problem of overmerging in the very central regions of the host. However, by tracking satellites rather than identifying them at separate time snapshots of the simulation we learned that this problem is *not* overmerging in the conventional sense. The objects are in fact present and simulated properly, but their densities have insufficient contrast to be picked up by a simple “finder”. Only when tracking them in time from (at best their very own) formation time were we able to quantify their existence as close as 5% of $r_{\text{vir}}^{\text{host}}$ to the cuspy centre. We do not intend to question the credibility of other (most excellent) halo finders such as SKID though. We rather pointed out that the results in the central region are subject to subtleties that can be most easily avoided by tracking satellites.

It has recently been pointed out by Taylor et al. (2003) that the radial distribution of the Milky Way’s satellite galaxies does not reconcile with the predictions of semi-analytical models of galaxy formation and cosmological simulations, respectively, which has been confirmed by Kravtsov et al. (2004). Even though there is quite a prominent substructure population in the simulations it is mostly clustered in the outer regions of the host whereas the Milky Way satellites are preferentially found closer in. It remains unclear if this poses a new challenge to the CDM structure formation scenario or simply reflects what we presented in this study. Namely, identifying substructure halos that lie close to the centre of the host is intrinsically challenging and might be overcome by actually *tracking* the satellites rather than *finding* them.

Finally, we further increase the statistics to suggest that anti-bias of the satellite distribution is a common property of the satellite distribution, perhaps even universal. However, this antibias is still most likely a relic of numerical overmerging. A convergence study for the satellite populations is critical in resolving this issue and reconciling the lensing observations. However, one very interesting result is the continued self-similarity in the dark matter distribution, the satellite radial distribution is common, once again perhaps “universal” even though the number of substructure satellites changes, reminiscent of the universal density profile of the underlying host.

9 ACKNOWLEDGMENTS

The simulations presented in this paper were carried out on the Beowulf cluster at the Centre for Astrophysics & Supercomputing, Swinburne University. We acknowledge the financial support of the Australian Research Council, the Swinburne Research Development Grant scheme, and Mike Dopita. Finally, we wish to thank Chris Power for helpful correspondences.

REFERENCES

- Aarseth, S. J., MNRAS **126**, 223 (1963)
 Bertschinger, E., Gelb, J. M.,
 Computers in Physics **5**, 164 (1991)
 Barnes, J. E., Hut, P., Nature **324**, 446 (1986)
 Bryan, G. L., Norman, M. L., ApJ **495**, 80 (1998)
 Bullock J., Kolatt T.S., Sigad Y., Somerville R.S., Kravtsov A.V., Klypin A.A., Primack J.R., Dekel A., MNRAS **559**, 321 (2001)
 Dalal, N., Kochanek, C. S., ApJ **572**, 25 (2002)
 Davis, M., Efstathiou, G., Frenk, C. S., White, S. D. M., ApJ **292**, 371 (1985)
 De Lucia, G., Kauffmann, G., Springel, V., White, S., astro-ph/0306205
 Efstathiou, G., Davis, M., Frenk C.S., White S.D.M., ApJ Suppl. **57**, 241 (1985)
 Franx M., Illingworth G., de Zeeuw T., ApJ **383**, 112 (1991)
 Frenk C.S., White S.D.M., Davis M., Efstathiou G., ApJ **327**, 507 (1988)
 Ghigna, S., Moore, B., Governato, F., Lake, G., Quinn, T., Stadel, J. MNRAS **300**, 146 (1998)
 Ghigna, S., Moore, B., Governato, F., Lake, G., Quinn, T., Stadel, J. MNRAS **544**, 616 (2000)
 Gill, S.P.D., Knebe, A., Gibson, B.K., Dopita, M.A., astro-ph/0311202
 Gill, S.P.D., Knebe, A., Gibson, B.K. 2004b, in preparation
 Gingold R.A., Monaghan J.J., MNRAS **181**, 375 (1977)
 Gleb, J. M., Bertschinger, E., ApJ **436**, 467 (1994)
 Götz, M., Huchra, J. P., Branderberger, R. H., astro-ph/9811393
 Groth, J. E., Peebles, P. J. E., ApJ **217**, 385 (1977)
 Hayashi, E., Navarro, J., Taylor, J., Stadel, J., Quinn, T., ApJ **584**, 541 (2003)
 Klypin A.A., Shandarin, S. F., MNRAS **204**, 891 (1983)
 Klypin A.A., Holtzman J., astro-ph/9712217
 Klypin A. Gottlober, S., Kravtsov A., Khoklov, A., ApJ **516**, 530 (1999)
 Klypin A., Kravtsov A., Valenzuela O., Prada, F., ApJ **522**, 82 (1999)
 Knebe A., Green A., Binney J., MNRAS **325**, 845 (2001)

- Kravtsov A. V., Klypin A. A., Khokhlov A. M.,
ApJ Suppl. **111**, 73 (1997)
- Kravtsov A. V., Gnedin O. Y., Klypin A. A., ApJ submitted,
astro-ph/0401088
- Lacey C., Cole S., MNRAS **281**, 716 (1996)
- Lucy L.B., Astron. J. **82**, 1013 (1977)
- Monaghan J.J., Ann. Rev. A & A **30**, 543 (1992)
- Moore, B., Katz, N., Lake, G., ApJ **457**, 455 (1996)
- Moore, B., Ghigna, S., Governato, F., Lake, G., Quinn, T., Stadel,
J., Tozzi, P., ApJ Lett. **524**, 19 (1999)
- Navarro J., Frenk C.S., White S.D.M., ApJ **490**, 493 (1997)
(NFW)
- Okamoto, T., Habe, A., ApJ **516**, 591 (1999)
- Peebles, P. J. E., Astron. J. **75**, 13 (1970)
- Suginohara, T., Suto, Y., ApJ **396**, 395 (1992)
- Suisalu, S., Saar, E., MNRAS **274**, 287 (1995)
- Summers, F., Davis, M., Evrard, A., ApJ **454**, 1 (1995)
- Suto, Y., Cen, R., Ostriker, J., ApJ **395**, 1 (1992)
- Taylor, J. E., Silk, J., Babul, A., **astro-ph/0312086**
- Tormen, G., Bouchet, F., White, S., MNRAS **286**, 865 (1997)
- van Kampen, E., MNRAS **273**, 295 (1995)
- Villumsen, J., V., ApJ Suppl. **71**, 407 (1989)
- Weinberg, D., Hernquist, L., Katz, N., ApJ **477**, 8 (1997)